www.sciencemag.org/content/363/6434/1435/suppl/DC1

Supplementary Material for

Chirally coupled nanomagnets

Zhaochu Luo*, Trong Phuong Dao, Aleš Hrabec, Jaianth Vijayakumar, Armin Kleibert, Manuel Baumgartner, Eugenie Kirk, Jizhai Cui, Tatiana Savchenko, Gunasheel Krishnaswamy, Laura J. Heyderman*, Pietro Gambardella*

*Corresponding author. Email: zhaochu.luo@psi.ch (Z.L.); laura.heyderman@psi.ch (L.J.H.); pietro.gambardella@mat.ethz.ch (P.G.).

Published 29 March 2019, *Science* **363**, 1435 (2017)
DOI: 10.1126/science.aau7913

This PDF file includes:

Materials and Methods

The magnetic films were deposited using dc magnetron sputtering at a base pressure $< 2 \times 10^{-8}$ Torr and deposition pressure of 3 mTorr. Continuous films of Pt(6 nm)/Co(1.6 nm)/Al (2 nm) were milled with Ar ions through a PMMA mask patterned by electron-beam lithography to produce elements of varying sizes. In order to define the IP region, a thin protective layer of Ta (2 nm), patterned by electron-beam lithography, was deposited on top of the Al layer. Finally, using a gentle oxygen plasma process with low power of 30 W and oxygen pressure of 10 mTorr, the top Al layer not protected by Ta was oxidized to induce perpendicular magnetic anisotropy. The different anisotropies, with out-of-plane (OOP) exposed regions and in-plane (IP) Ta-covered regions, were confirmed with polar Magneto-Optic Kerr Effect (MOKE) measurements (Fig. S1).

Magnetic imaging was performed using x-ray photoemission electron microscopy (X-PEEM) and magnetic force microscopy (MFM). X-PEEM was performed at the Surface/Interface Microscopy (SIM) beamline of the Swiss Light Source, Paul Scherrer Institute (*38*). Element-specific magnetic information was obtained using x-ray magnetic circular dichroism (XMCD) and tuning the x-ray photon energy to the L_3 absorption edge of Co. Images with magnetic contrast were obtained by pixelwise division of the intensities of two images $I(C^+)/I(C^-)$, which were acquired from the same sample region with positive and negative x-ray helicity, C^+ and C^-, respectively.

The MFM measurements were performed using tips coated with CoCr that are sensitive to the out-of-plane magnetization. For samples measured with MFM, we used PMMA as a protective layer (instead of Ta) to mask the Co during oxygen plasma treatment. We then removed the PMMA mask with acetone to obtain a flat surface for the MFM measurements, so eliminating the influence of topography on the magnetic contrast. Subsequently, in order to minimize the influence of the stray field from the MFM tip, we spin coated a thin PMMA layer (~20 nm) on the samples to increase the distance between the tip and the nanomagnets.

For the fabrication of the samples for electrical measurements (main process steps shown in Fig. S2), first alignment markers were fabricated and then the Pt(6 nm)/Co(1.6 nm)/Al (2 nm) layers were patterned onto a 1 μm-wide Hall cross using electron-beam lithography. Using a PMMA mask, the Co/Al layers were patterned into elements using Ar ion milling. The deposition of the protective Ta layer and selective oxidation to define the IP and OOP regions were performed as described above. Finally, a set of Cr(5 nm)/Au(50 nm) electrodes were fabricated by electron-beam lithography. For electrical measurements, the devices were connected to a source meter (Keithley 6221) and volt-meter (Keithley 2182) by wire bonding. All of the electrical measurements were performed at room temperature.

Supplementary Text

S1. In-plane magnetic field measurements

To further characterise the switching process of an OOP-IP element in an external magnetic field and differentiate the anomalous Hall effect associated with the OOP region from the planar Hall effect associated with the IP region, we performed Hall resistance measurements for different orientations of the magnetic field in the *x*-*y* plane (Fig. S3). In the following, the magnetization of the OOP and IP regions are indicated as M_{OOP} and M_{IP}, respectively, φ is the azimuthal angle of the in-plane magnetic field, and

$$R_{xy} = R_{\mathrm{AHE}} M_z + R_{\mathrm{PHE}} M_x M_y \tag{S1}$$

is the Hall resistance due to the anomalous Hall effect (AHE) and planar Hall effect (PHE), with coefficients R_{AHE} and R_{PHE}, respectively, and $M_i = \left(\vec{M}_{\mathrm{OOP}} + \vec{M}_{\mathrm{IP}}\right) \cdot \hat{\imath}$, where $\hat{\imath} = \hat{x}, \hat{y}, \hat{z}$ (see Fig. S3A). If the applied in-plane magnetic field is too weak to significantly tilt the OOP magnetization away from the *z* axis, R_{xy} has a constant offset $\pm R_{\mathrm{AHE}} M_{\mathrm{OOP}}$ due to the anomalous Hall effect from the OOP region and a φ-dependent contribution due to the planar Hall effect from the IP region. The easy axis of the IP region is determined by shape anisotropy and is parallel to the long axis of the element (*y*-axis).

Firstly, to confirm the contribution from the planar Hall resistance to R_{xy}, a control device consisting of a single IP element was fabricated and measured as a function of in-plane magnetic field. When the magnetic field is applied in-plane along the easy-axis of the element (φ = 90°), the magnetization is either parallel or antiparallel to *y*, such that $M_x = 0$, $M_y = \pm M_{\mathrm{IP}}$. The planar Hall resistance vanishes and no Hall resistance hysteresis is observed (see the curve measured at φ = 90° in Fig. S3B). When the in-plane magnetic field is non-collinear with the easy-axis, the magnetization deviates from the easy-axis, such that $M_x, M_y \neq 0$. The planar Hall resistance from the IP region will thus contribute a hysteretic signal with two jumps (see, *e.g.*, the curves measured at φ = 120° and 60° in Fig. S3B). The planar Hall effect $R_{xy} \propto \sin(2\varphi_{\mathrm{M}})$ has maxima at φ_{M} = 45° and 225°, and minima at φ_{M} = 135° and 315°, where φ_{M} is the azimuthal angle of the in-plane magnetization that is determined by the combination of external magnetic field and shape anisotropy (Fig. S3C). For 90° < φ < 180°, four different states, corresponding to the magnetization directions ***a***, ***b***, ***c*** and ***d*** schematically shown in Fig. S3C, give rise to the jumps observed in the Hall measurement curves (Fig. S3B). The Hall resistance jumps ***b***-***c*** and ***d***-***a*** indicate the switching of M_y. For example, at the switching point ***b***, $-M_y$ is switched to $+M_y$. As the equilibrium magnetization direction is intermediate between the easy axis and external field, the magnetization will then switch to direction ***c***. Because the planar Hall resistance at point ***b*** is larger than that at point ***c***, a Hall resistance jump appears. A similar reasoning explains the Hall resistance curves measured for 0° < φ <

90°, with the planar Hall resistance jumps in this case having opposite sign relative to 90° < φ < 180°.

In contrast to the single IP element, the Hall resistance loops of a coupled OOP-IP element, shown in Fig. S3D, have both anomalous and planar Hall contributions (see Eq. S1), even when the external field is applied in-plane. When the magnetic field points along the easy-axis of the IP region (φ = 90°), the planar Hall resistance vanishes and the observed jumps result from the anomalous Hall resistance, which indicates the switching of the OOP region. When the in-plane magnetic field is tilted with respect to the IP easy-axis ($\varphi \neq$ 90°), the Hall resistance is a combination of the symmetric and antisymmetric planar and anomalous Hall resistances, respectively. At zero magnetic field, when the IP magnetization points along $-y$ (←), the Hall resistance is always larger than the Hall resistance for IP magnetization pointing along $+y$ (→). This offset is due to anomalous Hall resistance of the OOP region and demonstrates that the OOP magnetization is controlled by the IP magnetization, which is consistent with the ↑← and ←↓ chiral configurations. Note that, when the magnetic field is applied at $\varphi \neq$ 90°, the planar and anomalous Hall resistance jumps coincide. Hence, for an in-plane magnetic field, the OOP region switches simultaneously with the IP region.

S2. Macrospin model of coupled OOP-IP elements

For regions whose size is below the critical size for single domain behavior, we model the magnetizations of the OOP and IP regions as two macrospins. The total energy of an OOP-IP element under an external magnetic field is thus given by the sum of the Zeeman energy and chiral coupling energy due to the Dzyaloshinskii-Moriya interaction (DMI):

$$E = -\vec{M}_{\mathrm{OOP}} \cdot \vec{H}_{\mathrm{ext}} - \vec{M}_{\mathrm{IP}} \cdot \vec{H}_{\mathrm{ext}} - \vec{D} \cdot (\vec{M}_{\mathrm{OOP}} \times \vec{M}_{\mathrm{IP}}), \tag{S2}$$

where $\vec{H}_{\mathrm{ext}}$ and $\vec{D}$ are the external magnetic field and the DMI vector, respectively. Considering all four magnetization configurations, the total energy can be written as:

$$\begin{aligned} E_{\uparrow\rightarrow} &= -M_{\mathrm{OOP}} \cdot H_{\mathrm{ext}} \cos\theta - M_{\mathrm{IP}} \cdot H_{\mathrm{ext}} \sin\theta, \\ E_{\downarrow\rightarrow} &= M_{\mathrm{OOP}} \cdot H_{\mathrm{ext}} \cos\theta - M_{\mathrm{IP}} \cdot H_{\mathrm{ext}} \sin\theta - E_{\mathrm{DM}}, \\ E_{\uparrow\leftarrow} &= -M_{\mathrm{OOP}} \cdot H_{\mathrm{ext}} \cos\theta + M_{\mathrm{IP}} \cdot H_{\mathrm{ext}} \sin\theta - E_{\mathrm{DM}}, \\ E_{\downarrow\leftarrow} &= M_{\mathrm{OOP}} \cdot H_{\mathrm{ext}} \cos\theta + M_{\mathrm{IP}} \cdot H_{\mathrm{ext}} \sin\theta, \end{aligned} \tag{S3}$$

where $E_{\mathrm{DM}} = -\vec{D} \cdot (\vec{M}_{\mathrm{OOP}} \times \vec{M}_{\mathrm{IP}})$ is the coupling energy due to the DMI and θ is the angle between H_{ext} and the surface normal. According to the experimental results, the ↓→ and ↑← configurations are low energy states. In our model, we assume that, if the energy difference between two configurations is larger than the energy barrier separating them,

the magnetic configuration will be switched to the lower energy state. We differentiate the following four cases:

(i) For θ = 0°, the magnetic field $H_{ext} = H_z$ only affects the Zeeman energy of the OOP region. We consider the IP magnetization to be → and start with the DMI-favorable configuration ↓ →. The total energies of the different configurations are shown in Fig. S4A. With increasing H_z, the OOP magnetization will switch at the critical field:

$$H_{C1} = \frac{\Delta E_{OOP} + E_{DM}}{2M_{OOP}} \triangleq H_{z+}^{*}, \tag{S4}$$

where ΔE_{OOP} is the energy barrier for switching the OOP magnetization. At this field, the energy difference between ↓ → and ↑ → is higher than ΔE_{OOP}. The magnetization configuration is thus switched to the DMI-unfavorable ↑ → configuration from the ↓ → configuration. When decreasing H_z, the magnetic configuration will be switched back to the DMI-favorable ↓ → configuration at the critical field:

$$H_{C2} = -\frac{\Delta E_{OOP} - E_{DM}}{2M_{OOP}} \triangleq -H_{z-}^{*}. \tag{S5}$$

(ii) For θ = 90°, $H_{ext} = H_y$ only affects the Zeeman energy of the IP magnetization. The total energies of the different magnetization configurations are shown in Fig. S4B. We start with the DMI-favorable configuration ↑ ←. With increasing H_y, because the energy difference between ↑ → and ↑ ← is larger than the switching energy barrier of the IP magnetization ΔE_{IP}, the IP magnetization will be switched to → at the critical field:

$$H_{C3} = \frac{\Delta E_{IP} + E_{DM}}{2M_{IP}} \triangleq H_{y}^{*}. \tag{S6}$$

As shown in the experiment, due to the strong chiral coupling between the OOP and IP magnetizations, the OOP magnetization switches simultaneously with the IP magnetization to minimize the total energy. Therefore, the magnetization is switched to the DMI-favorable configuration ↓ →. The condition for this simultaneous switching is $E_{DM} > \Delta E_{OOP}$.

(iii) For 0° < θ < 90°, when θ is close to 90° (left panel, Fig. S4C), the switching situation is similar to that of θ = 90° and the switching field is given by:

$$H_{C3} = \frac{\Delta E_{IP} + E_{DM}}{2M_{IP}\sin\theta} = \frac{H_{y}^{*}}{\sin\theta}. \tag{S7}$$

This situation corresponds to the Type I behavior shown in Fig. 2B of the main text.

For intermediate θ values (middle panel, Fig. S4C), when the magnetic field is large, the Zeeman energy of the OOP magnetization becomes large enough to switch the OOP region against the chiral coupling energy, switching from ↓ → to ↑ → at the critical field:

$$H_{\mathrm{C1}} = \frac{\Delta E_{\mathrm{OOP}} + E_{\mathrm{DM}}}{2M_{\mathrm{OOP}}\cos\theta} = \frac{H^{*}_{z+}}{\cos\theta}. \tag{S8}$$

Starting from the high field ↑ → configuration and decreasing the applied field, the OOP magnetization switches to ↓ as the Zeeman energy of the OOP magnetization becomes lower than E_{DM} - ΔE_{OOP} at the critical field:

$$H_{\mathrm{C2}} = -\frac{\Delta E_{\mathrm{OOP}} - E_{\mathrm{DM}}}{2M_{\mathrm{OOP}}\cos\theta} = -\frac{H^{*}_{z-}}{\cos\theta}. \tag{S9}$$

Thus, below H_{C2}, the magnetic state corresponds to the DMI-favorable ↓ → configuration. Reducing the field to zero and reversing it to negative values leads to switching of the IP magnetization from → to ← and the simultaneous switching of the OOP magnetization from ↓ to ↑ due to the chiral coupling at H_{ext} = -H_{C3}. Thus, for -H_{C1} < H_{ext} < -H_{C3}, the magnetic state corresponds to the DMI-favorable ↑ ← configuration. Finally, at H_{ext} = -H_{C1} the OOP magnetization is forced by the magnetic field to point ↓ and the magnetic state corresponds to the DMI-unfavorable ↓ ← configuration. This switching sequence corresponds to the Type II behavior reported in Fig. 2B of the main text.

When θ is close to 0° (right panel, Fig. S4C), the Zeeman energy of the OOP magnetization becomes dominant. At large magnetic field, the magnetic configuration is the DMI-unfavorable ↑ → configuration. With decreasing magnetic field, as the Zeeman energy of the OOP magnetization becomes lower than E_{DM} - ΔE_{OOP}, the magnetic state switches back to the DMI-favorable ↓ → configuration at the critical field H_{C2}. When the magnetic field is large and the Zeeman energy of the IP magnetization larger than ΔE_{IP} + E_{DM}, the IP magnetization will switch at the critical field H_{C3}. This switching sequence corresponds to the Type III behavior reported in Fig. 2B of the main text.

(iv) For 90° < θ < 180°, when θ is close to 90° (left panel, Fig. S4D), the switching sequence is similar to that of θ = 90° and the switching field is H_{C3} (Type I behavior). If θ is close to 180° (right panel, Fig. S4D), the Zeeman energy of the OOP magnetization becomes dominant. With increasing magnetic field, the OOP magnetization will be switched first at the critical field H_{C1}. When the magnetic field is large, because the magnetic configuration is switched to the DMI-unfavorable ↓ ← configuration, the Zeeman energy of the IP magnetization required to switch to the DMI-favorable ↓ → configuration is ΔE_{IP} - E_{DM}, and the switching magnetic field is

$$H_{C4} = \frac{\Delta E_{IP} - E_{DM}}{2M_{IP}\sin\theta} = \frac{H^*_{y-}}{\sin\theta}. \tag{S10}$$

The experimental values of the critical switching fields of an OOP-IP element are shown in a H_y-H_z diagram in Fig. 2D. The fields lie close to the lines predicted by Eqs. (S4 to S9), demonstrating that our macrospin model captures the OOP-IP chiral coupling rather accurately. Using this model, we can derive all the relevant energy parameters E_{DM}, ΔE_{OOP} and ΔE_{IP} from the switching fields. According to the experimental data, we find $H^*_{z+} = (\Delta E_{OOP} + E_{DM})/ 2M_{OOP} = (3.7 \pm 0.4) \times 10^2$ Oe, $H^*_{z-} = (\Delta E_{OOP} - E_{DM})/ 2M_{OOP} = -63 \pm 9$ Oe and $H^*_y = (\Delta E_{IP} + E_{DM})/ 2M_{IP} = (1.60 \pm 0.07) \times 10^2$ Oe. Taking a Co saturation magnetization of 1.43 MA/m, and taking the areas of the OOP and IP regions, we estimate that $M_{OOP} = 1.30\times10^{-17}$ A·m^2 and $M_{IP} = 1.51\times10^{-16}$ A·m^2. The energies E_{DM}, ΔE_{OOP}, and ΔE_{IP} are thus 3.5 ±0.3 eV, 2.5 ±0.3 eV and 26 ±1 eV, respectively. It should be noted that the switching energy barriers of each region, OOP and IP increase quadratically with size, whereas the chiral coupling energy increases linearly with size. The chiral coupling effect is thus significant only for small elements, as discussed in the main text and shown in Fig. 2E.

Alternatively, we can estimate the chiral coupling by calculating the energy gain due to the DMI for the domain wall separating the OOP and IP regions. The calculation is analogous to that presented in Ref. 20 for chiral domain walls, except that here we deal with a 90° rather than a 180° domain wall. Assuming that the magnetization rotates homogeneously across the wall, the DMI energy of the wall can be written as

$$\begin{aligned} E_{DW} &= \int_{\Omega_{DW}} D(m_z \frac{\partial m_x}{\partial x} - m_x \frac{\partial m_z}{\partial x}) dV \\ &= \int_{\Omega_{DW}} D(\cos\frac{\pi x}{2W_{DW}} \cdot \frac{\pi}{2W_{DW}} \cdot \cos\frac{\pi x}{2W_{DW}} - \sin\frac{\pi x}{2W_{DW}} \cdot -\frac{\pi}{2W_{DW}} \cdot \sin\frac{\pi x}{2W_{DW}})\, dV \\ &= \int_{\Omega_{DW}} \frac{\pi D}{2W_{DW}}\, dV = \frac{\pi}{2} Dlt, \end{aligned} \tag{S11}$$

where Ω_{DW}, W_{DW}, l and t are the integration region of the 90° domain wall, domain wall width, domain wall length, and the thickness of the magnetic layer, respectively. The chiral coupling energy is the difference between the DMI energy of two walls with opposite chirality, namely $E_{DM} = 2E_{DW} = \pi Dlt$. Taking a typical DMI value of 1 mJ/m^2 for a thin Pt/Co film, the chiral coupling energy is 3.77 eV, which agrees well with E_{DM} = 3.5 ±0.3 eV derived experimentally from the analysis of the switching fields.

S3. Control measurements on isolated OOP elements

Control devices with isolated OOP elements were fabricated in parallel to the OOP-IP devices to ensure the reproducibility of all the deposition and processing parameters. First, we measured the control device with one isolated OOP element (Fig. S5A). The shape of the OOP element is the same as that of the OOP region in the coupled OOP-IP elements. However, in contrast to the OOP-IP elements, we find that the switching field of an isolated OOP element increases as the magnetic field is rotated from the OOP to the IP direction (Fig. S5B). Furthermore, the OOP magnetization cannot be switched at all if the external magnetic field is applied in-plane.

Additionally, we performed current-induced switching measurements on the isolated OOP element. As shown in Fig. S5C, for the current density employed in the present work (~5×10^{11} A/cm^2), the OOP magnetization can be switched only in the presence of a large in-plane magnetic field of 1.2 kOe applied parallel to the current. This is the typical behavior expected for spin-orbit torque-induced magnetization switching of an OOP element, for which the in-plane field is required in order to break the symmetry of the damping-like torque relative to the up and down magnetization directions (*21*,*22*,*27*,*28*). This result confirms that the field-free switching of the OOP magnetization is due to the chiral coupling in the OOP-IP element. Furthermore, we find that the critical current density required to switch the OOP-IP element is around 4.7×10^{11} A/cm^2, whereas the critical current density required to switch the isolated OOP element is >5.2×10^{11} A/cm^2, demonstrating that the chiral coupling improves the switching efficiency.

S4. Estimate of the dipolar coupling energy between OOP elements

In order to test the influence of dipolar coupling, we measured a control device consisting of two OOP elements separated by a distance equal to the length of the IP region of the OOP-IP-OOP element used for the measurements presented in Fig. 3C of the main text. The Hall resistance measurements of the control device, shown in Fig. S6A, do not show evidence of antiparallel coupling between the two OOP elements.

A rough estimation of the dipolar coupling energy between the two OOP elements can be obtained by considering two point-like dipoles placed at the center of each element at a distance r from each other. In this case, the ratio between the dipolar coupling energy ($E_{\mathrm{dip}} = E_{\uparrow\uparrow} - E_{\downarrow\uparrow}$) and the switching energy barrier is

$$\frac{E_{\mathrm{dip}}}{\Delta E_{\mathrm{OOP}}} = 2\frac{\mu_0 M^2}{4\pi r^3} / \Delta E_{\mathrm{OOP}} \sim 1.5\times10^{-3}, \tag{S12}$$

with $M = 3.30\times10^{-17}$ A·m^2 (for nanomagnet dimensions of 120 nm×120 nm×1.6 nm) and $r = L + w/2 + w/2 = 420$ nm, where L and w are the separation and width of the two elements, respectively. This ratio is several orders of magnitude smaller than the ratio $E_{DM}/\Delta E_{OOP} \approx 1.91$ that results from the chiral coupling in an OOP-IP-OOP element with the same dimensions, such as the one reported in Figs. 3A-C.

A better estimate of the dipolar coupling energy, particularly at small distances, is obtained by using a finite element method to simulate the dipolar field H_{dip} produced by one OOP element at the position of the second element. By assuming uniform OOP magnetization for both elements, the dipolar coupling energy is given by:

$$E_{dip} = 2\mu_0 \int_{\text{OOP element}} H_{dip} M dV \,. \tag{S13}$$

As shown in Fig. S6B, even for a close separation of $L = 10$ nm, $E_{dip} \approx 0.16\Delta E_{OOP}$. With such a small dipolar coupling, it is not possible to achieve the spontaneous antiferromagnetic state observed in the OOP-IP-OOP elements.

S5. Influence of the boundary shape between OOP and IP regions

The OOP-IP and OOP-IP-OOP elements reported in the main text have a straight boundary between the OOP and IP regions. In Fig. S7, we show that the chiral coupling remains strong for OOP-IP elements with different shaped boundaries. This behavior differs from the behavior of dipolar-coupled single-domain magnetic elements where the shape of the element influences the coupling strength. Moreover, this result implies that chiral coupling will not be significantly affected by edge defects resulting from the fabrication processes.

S6. Further X-PEEM analysis

In our X-PEEM measurement setup the incoming photons reach the sample at a grazing incidence angle of 16°. The XMCD contrast is proportional to $\boldsymbol{M}\cdot\boldsymbol{k}$, where $\boldsymbol{M}$ and $\boldsymbol{k}$ are the local magnetization and x-ray propagation vector, respectively. Thus, the magnetic contrast is larger for the IP magnetization than for the OOP magnetization. However, the Ta capping layer covering the IP region attenuates the IP magnetization signal. As the magnetization rotates across the element from ↓ to → (see Fig. S8A), the XMCD contrast should change from white to black. However, because the XMCD intensity of the IP region is attenuated by Ta, the measured XMCD contrast changes from white to dark-grey (Fig. S8A). The maximum dark contrast between the ↓ and → regions (Fig. S8A and S8B) corresponds to the OOP-IP domain wall, which is consistent

with the left-handed domain wall chirality expected from the DMI in Pt/Co/AlO_x. As the magnetization rotates from → to ↑, the measured XMCD contrast changes from dark-grey to black, as seen in the experimental images (Fig. S8B). Note that reversing the direction of the IP magnetization leads to the observation of opposite ↑← and ←↓ couplings (Fig. S8C).

The different nature of the IP and OOP magnetization contrast was further confirmed by imaging the samples at different azimuthal angles with respect to the incoming x-rays. In Fig. S9, it can be seen that the contrast due to the OOP magnetization remains unchanged, whereas the contrast due to the IP magnetization changes, going from dark-grey to grey and light-grey as the x-ray incidence angle varies from 0° to 90° and 180°, respectively.

S7. Micromagnetic simulations

Micromagnetic simulations were performed in order to confirm the picture obtained from the macrospin model presented in Section S2. The simulations were carried out with the MuMax^3 code (*40*) using a computation box containing 512×512×1 2 nm cells with the following magnetic parameters: saturation magnetization M_S = 0.9 MA/m, exchange constant A = 16 pJ/m and interfacial DMI constant D = -1.5 mJ/m^2. Note that the chosen parameters are slightly different from those obtained by the macrospin model. This discrepancy is attributed to the fact that the macrospin model does not include spatially-dependent features, such as the bending of the domain wall and the curling of the spins at the sample edges. Moreover, for simplicity, we consider a single set of parameters for the OOP and IP regions, even though some spatial variations are expected, for example, due to the material microstructure and inhomogeneous oxidation of the OOP region. The magnetic element of width w, depicted in Fig. S10A, is divided into two regions where the perpendicular anisotropy field H_K is set to zero in the 550 nm long IP region, whereas H_K is non-zero in the the OOP region (w-nm long). The dependence of the M_y and M_z components on the in-plane magnetic field H_y, shown in Fig. S10B for an element with w = 120 nm, reveals that the OOP and IP regions switch simultaneously up to the effective anisotropy field H_K=1700 Oe. For elements with stronger perpendicular anisotropy, the two components are no longer able to switch simultaneously and the IP region switches separately in response to an in-plane field. This is shown systematically in Fig. 2E of the main text: the black dots set the upper limit for the anisotropy field for the simultaneous switching. For elements with larger width, a multidomain state spontaneously develops, which is indicated by the red dots in Fig. 2E. The dependence of the M_z component on the out-of-plane magnetic field in Fig. S10C confirms the experimentally observed

switching behaviour. The lateral coupling shifts the hysteresis loops in a similar manner to exchange bias with the sign of the bias set by the sign of the DMI.

S8. Different designs of OOP-IP-OOP elements

Several OOP-IP-OOP designs were fabricated in order to test the coupling in structures with different shapes and dimensions. In Fig. S11A, an OOP-IP-OOP element with a 1 μm long IP region is shown. The Hall resistance measurements in Fig. S11B, analogous to those reported in Fig. 3C of the main text, show that two OOP regions are antiferromagnetically coupled through the long IP region. The synthetic antiferromagnetic state is controlled by the preset direction of IP magnetization. In Fig. S11C, an OOP-IP-OOP element with a curved IP patterned region is shown. Also, in this case we observe a robust antiferromagnetic state corresponding to either the ↓→↑ or ↑←↓ configuration, depending on the preset direction of the IP magnetization. With a curved IP region, it is possible to couple two distant OOP regions while bypassing other neighboring OOP elements, which provides additional freedom in the design of coupled nanomagnetic patterns.

S9. Synthetic skyrmions

The flexibility in the patterning of the OOP and IP elements means that coupled structures of arbitrary shape can be easily realized. Moreover, since these structures inherit the chirality of the coupling, we can design nontrivial topological magnetic structures. As an example, we realized a synthetic skyrmion consisting of two concentric OOP regions connected by an intervening IP ring, as shown in Fig. S12A. The diameter of the innermost OOP region is 150 nm and the IP ring is 50 nm wide. Due to the chiral coupling mediating the antiferromagnetic interaction between the OOP regions, the magnetic configuration at zero applied field is either ↑←↓ or ↓→↑, depending on the direction of the out-of-plane field used to initialize the state of the largest OOP region (Fig. S12B and S12C). The winding number of such a configuration is +1 whereas the topological charge is $Q = p(1\text{-}\cos\theta)/2 = \pm 1$, with p being the skyrmion polarity (*i.e.*, the magnetization orientation in the center) and θ the rotation angle of the magnetization taken from the center to the edge of the skyrmion. Control measurements performed on single OOP discs, reported in Fig. S12D to S12F, demonstrate that the synthetic skyrmion structure does not result from the minimization of magnetostatic interactions (*41*).

By patterning more IP rings, it is possible to create synthetic skyrmionic structures with exotic topological textures. Structures consisting of two to five IP rings separating concentric OOP regions with antiparallel magnetization are shown in Figure S13. The

topological charge of these structures alternates between 0 and +/-1 for even and odd numbers of IP rings, respectively. In all of these cases, the direction of the magnetization is preset by an external field applied out-of-plane, which determines the orientation of the largest OOP region. In contrast to skyrmions that form spontaneously in homogeneous bulk and thin film systems, these synthetic skyrmions do not move under the action of fields or current. Nevertheless, they provide an example of how chiral coupling can be used to induce exotic topological structures, which are stable in zero field, and are of interest for the investigation of high-frequency excitations of skyrmions, as well as for the generation and transmission of spin waves in magnonic crystals.

S10. Artificial Ising lattices and spin ices

Chirally coupled nanomagnets can also be used as building blocks to design complex interconnected systems that show unusual collective behavior, for example, in artificial spin ices. In order to demonstrate this point, we realized a mesoscopic version of the two-dimensional antiferromagnetic Ising model by fabricating an array of OOP elements on a square lattice connected by IP elements, as shown in Fig. S14A. The widths of the IP and OOP elements are 50 nm and 150 nm, respectively, which are small enough to ensure that the IP elements are single domain and that there is a strong nearest neighbor antiferromagnetic interaction between the OOP elements. After initializing the system by applying a saturating magnetic field in the out-of-plane direction and returning the field to zero, the chirally coupled array contains extended domains of antiferromagnetically ordered OOP elements (see MFM images in Fig. S14B and S14C). The remanent state of a control sample consisting of OOP elements with the same size and spacing, but without IP elements, consists of mostly OOP elements with magnetization aligned in the direction of the applied field, with only 0.4 % of neighboring elements having opposite magnetization. Here the dipolar coupling is too weak to give an antiparallel alignment of neighboring OOP elements. The size of the antiferromagnetic domains increases if the samples are subject to a magnetic field that is reduced from above saturation to zero field while rotating the sample about an in-plane axis as shown in the inset of Fig. S14D.

We can construct arrays of highly frustrated OOP macrospins by placing them on the sites of corner sharing triangles forming a kagome lattice. Here, the pairwise antiferromagnetic coupling of the neighboring spins cannot be satisfied simultaneously (Fig. S15A). A finite structure composed of Ising-like OOP elements placed on the sites of the kagome lattice and connected by short IP elements is shown in Figure S15B. The OOP elements have an X-like shape with 150 nm - wide crossed bars, and the connecting rectangular IP elements are 150 nm wide and 50 nm long. The chiral coupling between

the OOP elements, which results in frustrated antiferromagnetic interactions, prevents the system from attaining long-range order, resulting in a large number of nearly degenerate low-energy configurations. Four such configurations are shown in Fig. S15C to S15F, measured with MFM after demagnetization by rotating the sample in a magnetic field about the axis indicated in (B) while reducing the field strength from above saturation to zero.

These measurements demonstrate the possibility of assembling magnetic metamaterials composed of chirally coupled nanomagnets, each acting as a single macrospin, in arrays that have a well-defined geometry and size. Two-dimensional Ising lattices with nearest-neighbor interactions are one of the simplest models of interacting magnetic spins that show nontrivial behavior (*42*). These models are widely employed in theoretical studies of the critical behavior of cooperative spin systems, such as phase transitions and thermodynamic properties. Chirally coupled lattices open the way to the experimental observations of the correlated dynamics in artificial Ising lattices with strong antiferromagnetic interactions.

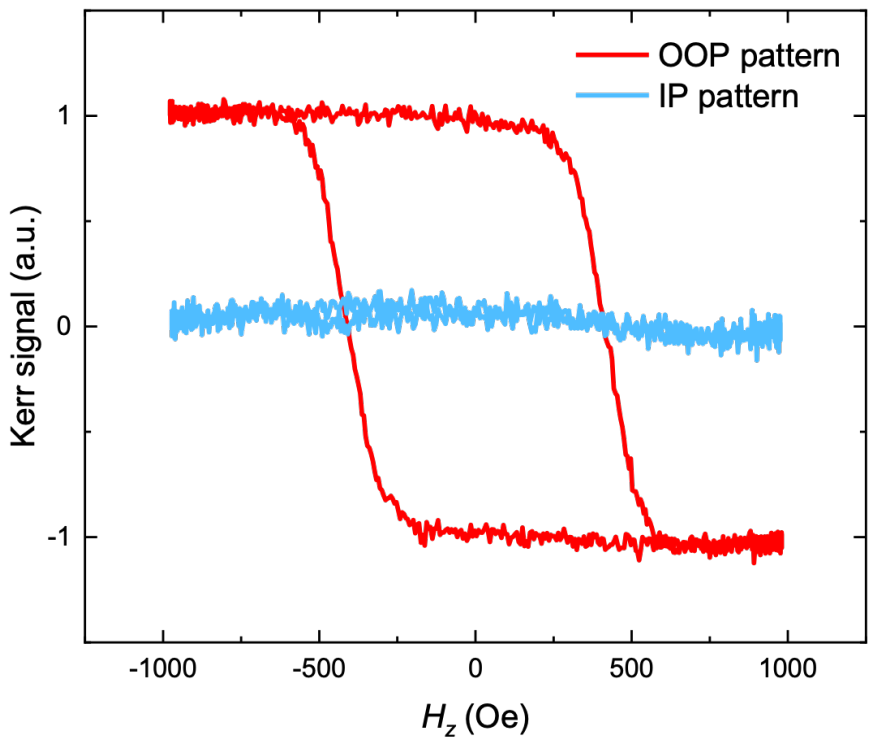

Fig. S1. Polar MOKE measurement of the OOP and IP regions as a function of out-of-plane magnetic field.

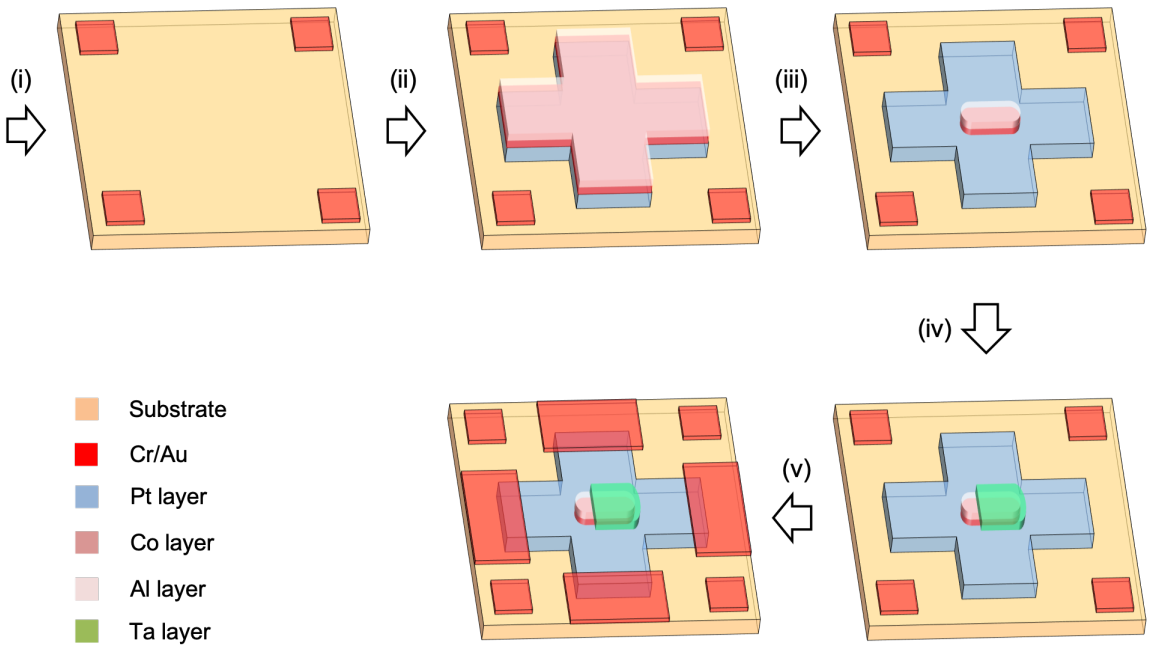

Fig. S2 Fabrication process steps for the OOP-IP devices employed in the electrical measurements. (i) Fabrication of alignment markers; (ii) fabrication of magnetic cross bar; (iii) ion milling of the magnetic element; (iv) deposition of the protective Ta layer; (v) deposition of the electrodes and oxidation in an oxygen plasma.

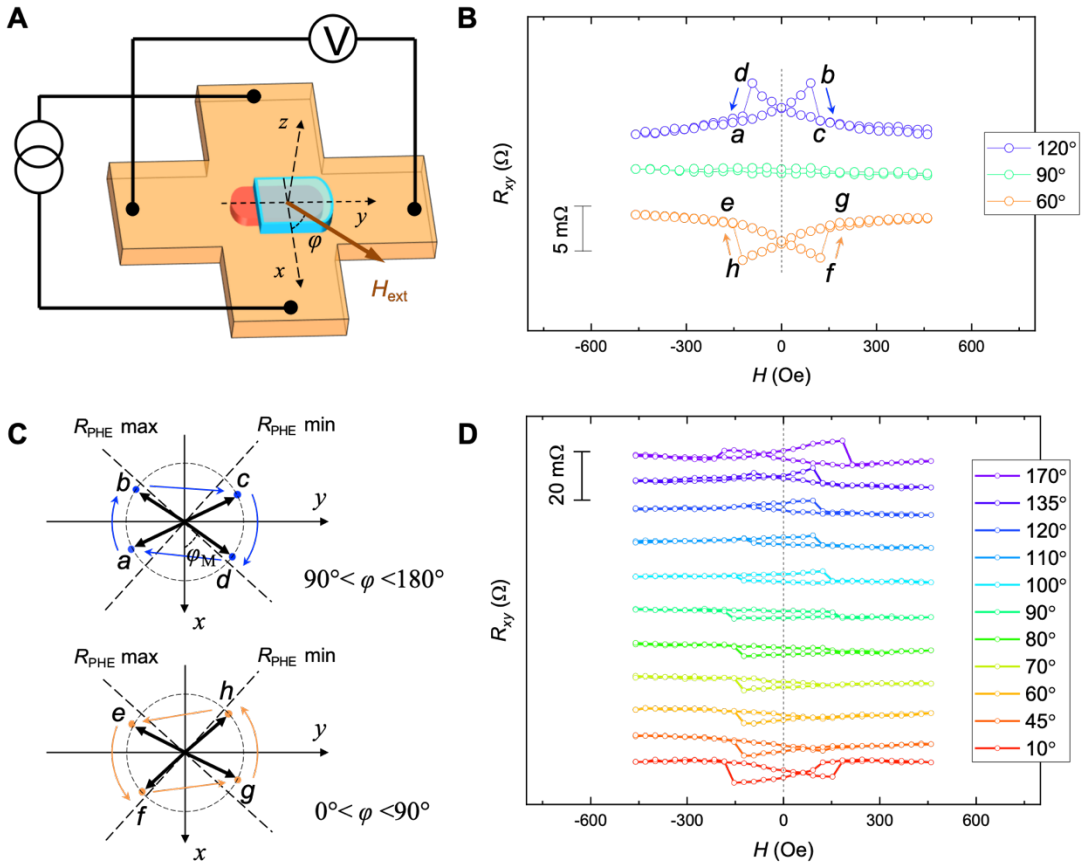

Fig. S3 Hall resistance measurements of a single IP element and of a coupled OOP-IP element as a function of magnetic field in the *x*-*y* plane: (A) Schematic of the setup and orientation of the in-plane magnetic field. (B) Hall resistance loops of a single IP element for different directions of the in-plane magnetic field. (C) Schematic of the in-plane magnetization directions corresponding to the switching of an IP element when applying a magnetic field at an angle φ relative to the x axis. The black arrows indicate the directions of the magnetization near the switching points. (D) Hall resistance loops of an OOP-IP element for different directions of the in-plane magnetic field.

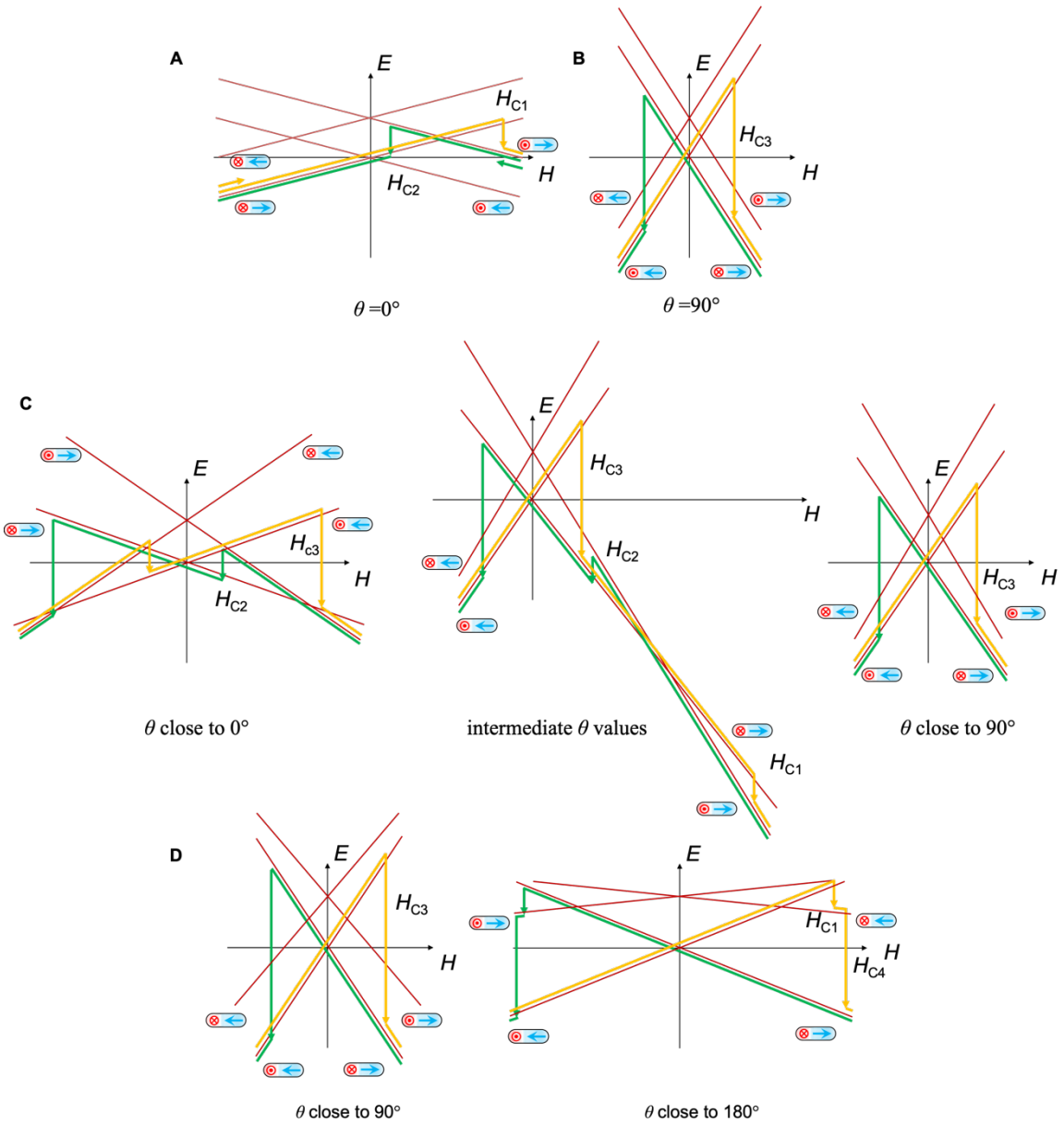

Fig. S4 Energy of different magnetization configurations of a coupled OOP-IP element as a function of applied magnetic field in the *y-z* plane. The polar angle of the applied field is (A) θ =0°, (B) θ =90°, (C) 0°< θ <90°, and (D) 90°< θ <180°. The red lines represent the energies of four different magnetic configurations according to Eq. S3. Yellow and green lines represent the energy paths for forward and backward magnetic field sweeps, respectively. The critical switching fields H_{C1} to H_{C4} are labeled for the positive sweeps.

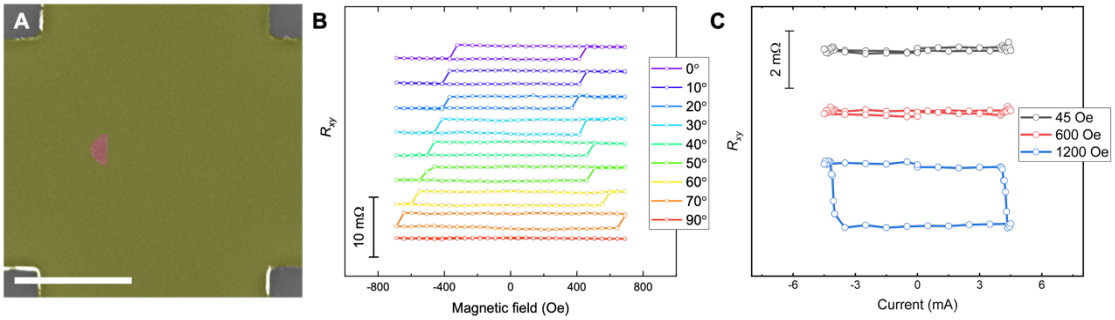

Fig. S5 Field- and current-induced switching of a single OOP element. (A) Scanning electron micrograph of a single OOP element on a Pt Hall cross. The scale bar is 500 nm. (B) Hall resistance of the single OOP element for different directions of the magnetic field in the *y*-*z* plane. (C) Current-induced switching for different magnetic fields applied along the *x* axis.

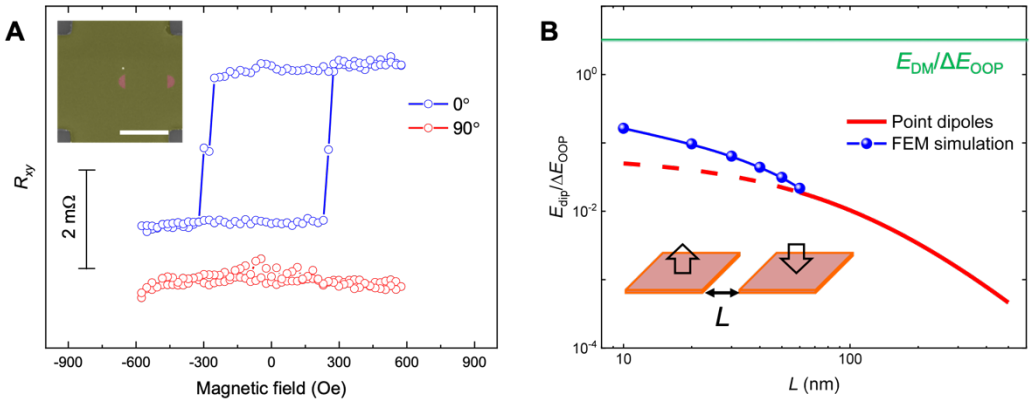

Fig. S6 Control measurement and estimate of the dipolar coupling energy between two separate OOP elements. (A) Hall resistance of two separate OOP elements (inset) as a function of out-of-plane and in-plane magnetic field. The scale bar in the inset corresponds to 500 nm. (B) Calculated ratio of the dipolar coupling energy relative to the OOP switching barrier for two separated OOP elements as a function of their separation *L*. The red and blue lines indicate estimates obtained using point-like dipoles and a finite element method, respectively. The size of the nanomagnet used for the simulations was 120 nm×120 nm×1.6 nm.

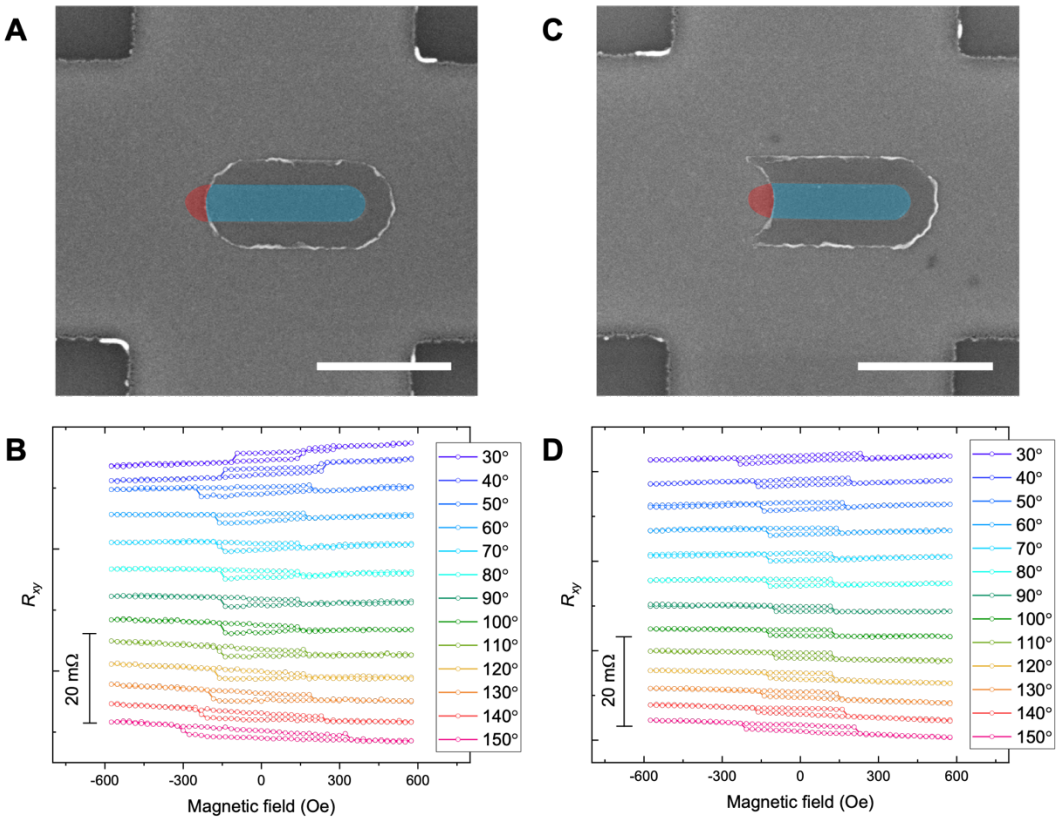

Fig. S7 Chiral coupling in OOP-IP elements with curved boundaries. (A) and (B) Scanning electron micrographs of OOP-IP elements with different boundary shapes. (C) and (D) Magnetic hysteresis loops of OOP-IP elements corresponding to (A) and (B) for different directions of the magnetic field in the *y*-*z* plane with the same definition of angle given in Fig. 1D of the main text. The scale bars are 500 nm.

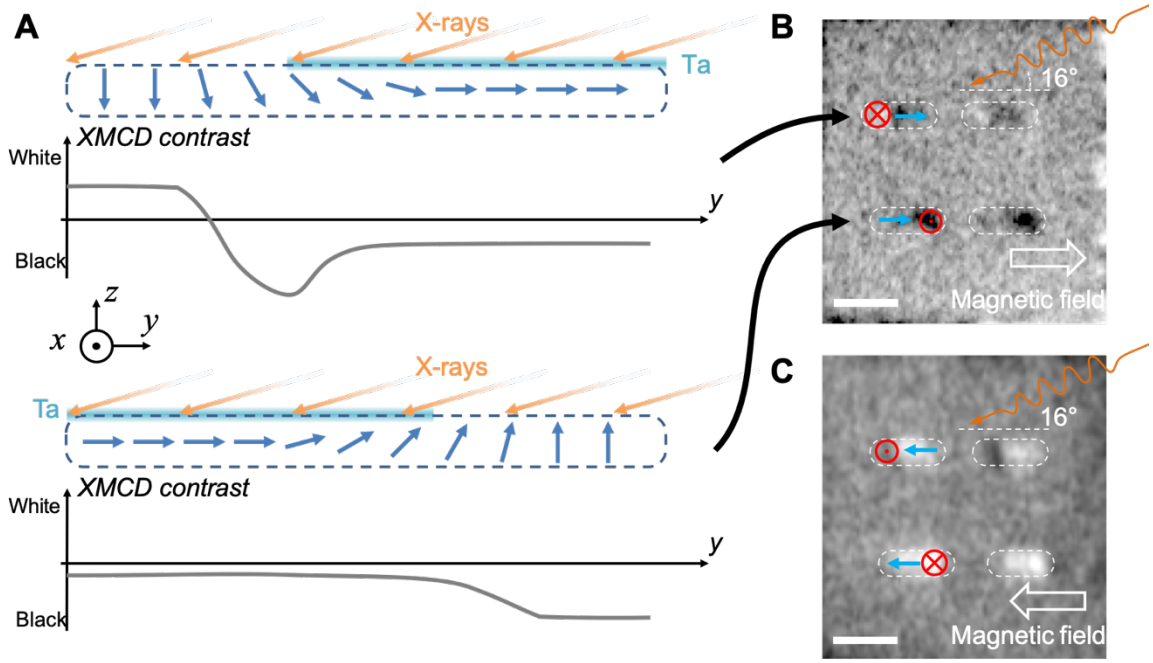

Fig. S8 XMCD contrast of OOP and IP magnetized regions. (A) Schematic of the ↓ → and → ↑ magnetic configurations of an OOP-IP element and their corresponding XMCD contrast. (B) and (C) X-PEEM images of the magnetic contrast of OOP-IP elements with opposite directions of the magnetization in the IP region. The directions of the incident x-rays and the magnetic field used to set the IP magnetization direction are indicated with arrows. The scale bars are 500 nm.

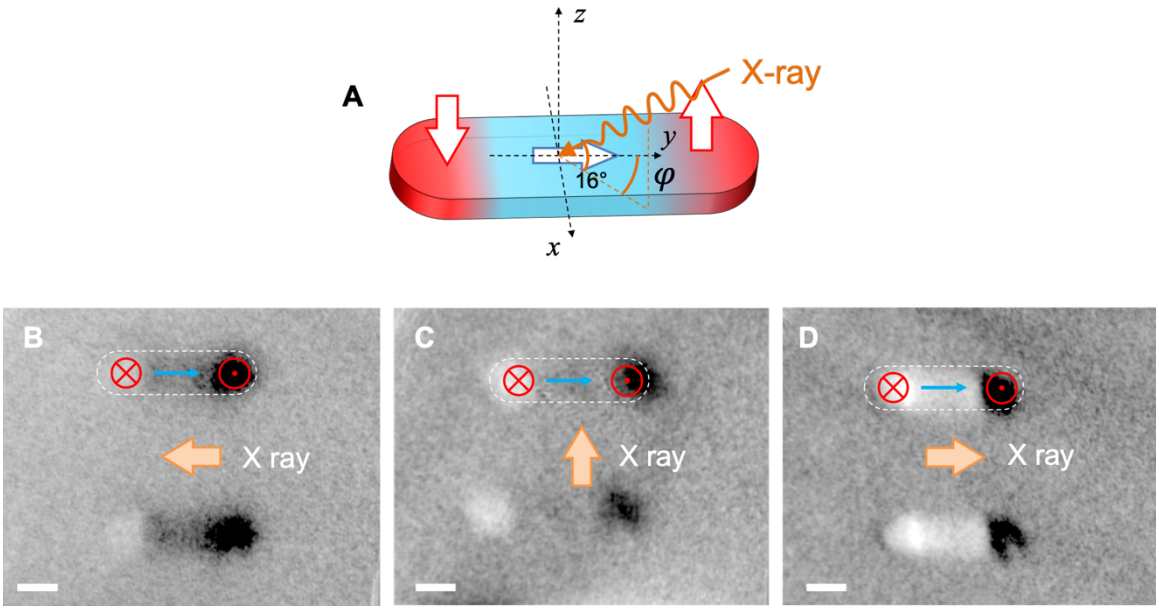

Fig. S9 X-PEEM magnetic contrast images of an OOP-IP-OOP element for different x-ray directions. (A) Measurement geometry. The X-PEEM magnetic contrast images of the two OOP-IP-OOP elements are measured for x-rays incident at an azimuthal angle φ of (B) 0°, (C) 90° and (D) 180°. The scale bars are 500 nm.

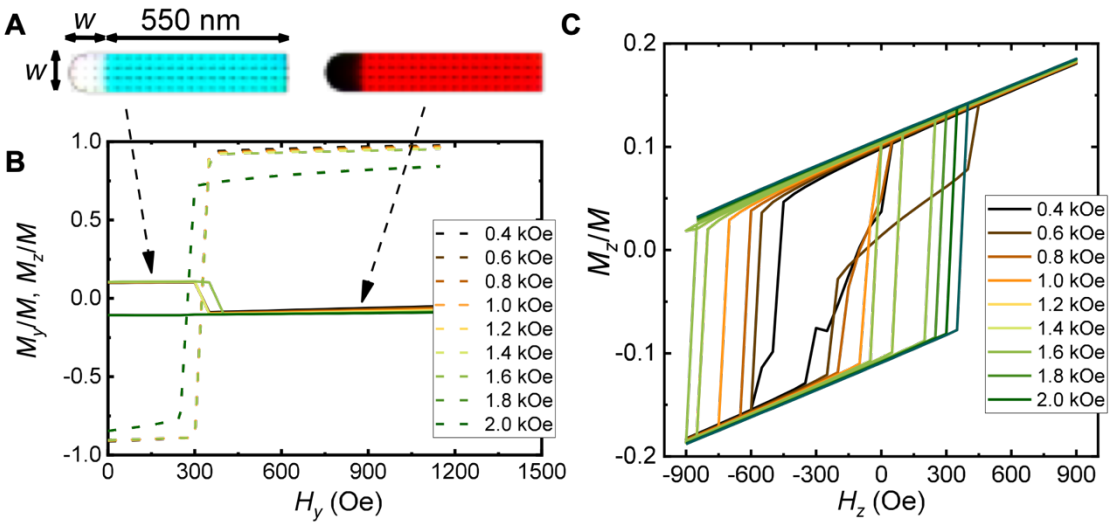

Fig. S10 Micromagnetic simulations of coupled OOP-IP elements. (A) Schematic of the magnetic element. The element size is defined by the width w. The IP region is 550 nm long. White and black colors correspond to the $+M_z$ and $-M_z$ components, respectively, whereas red and blue correspond to the $+M_y$ and $-M_y$ components. (B) M_y (dashed line) and M_z (solid line) as a function of in-plane magnetic field for various anisotropy fields and w = 120 nm. Note that the curves corresponding to anisotropy fields H_K < 1.6 kOe overlap each other. (C) Simulated hysteresis loops for elements with various anisotropy fields and w = 120 nm.

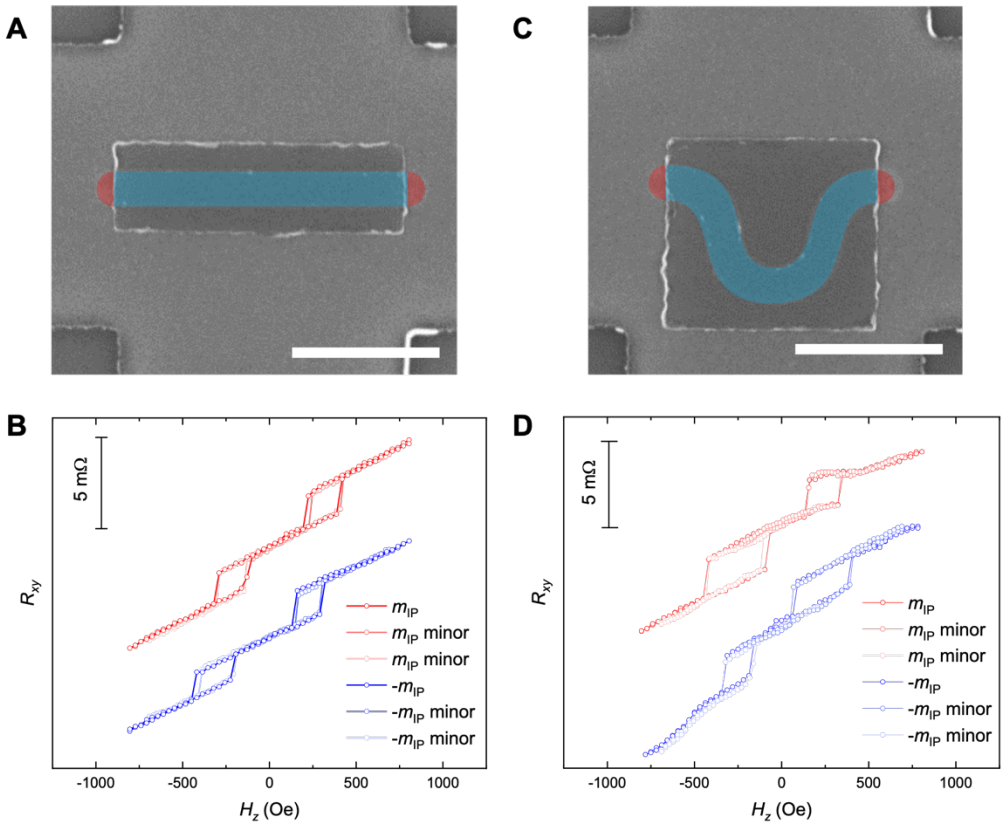

Fig. S11 Lateral synthetic antiferromagnetic state of OOP-IP-OOP elements connected by different IP regions. Scanning electron micrographs of OOP-IP-OOP elements with (A) a long IP region and (B) a curved IP region. (C) and (D) Magnetic hysteresis loops for (A) and (B) as a function of H_z. Minor loops for $H_z > 0$ and $H_z < 0$ are also shown and coincide with the full loops. The scale bars are 500 nm.

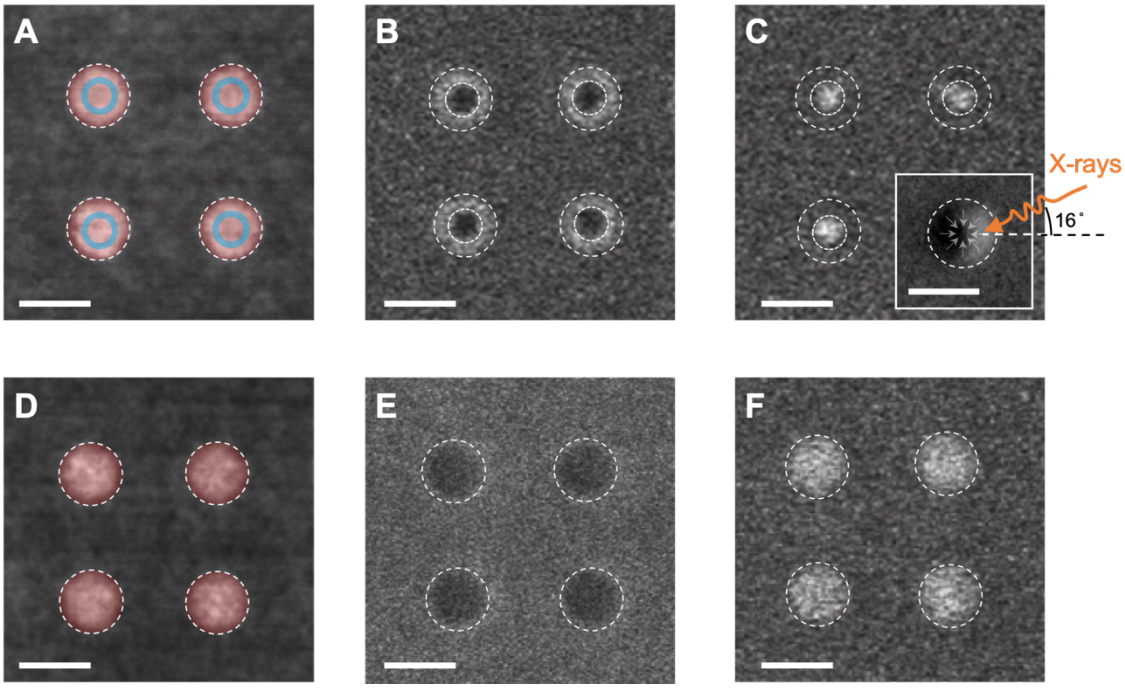

Fig. S12 Synthetic skyrmions. (A) False color atomic force microscopy image of synthetic skyrmions. The red and blue areas represent OOP and IP regions, respectively. (B) and (C) MFM images of synthetic skyrmions following the application of magnetic fields -H_z and +H_z, respectively. Inset: X-PEEM image of a synthetic skyrmion sensitive to IP magnetic contrast. (D) False color atomic force microscopy image of OOP discs. (E) and (F) MFM images of the discs following the application of magnetic fields -H_z and +H_z, respectively. The scale bars are 500 nm.

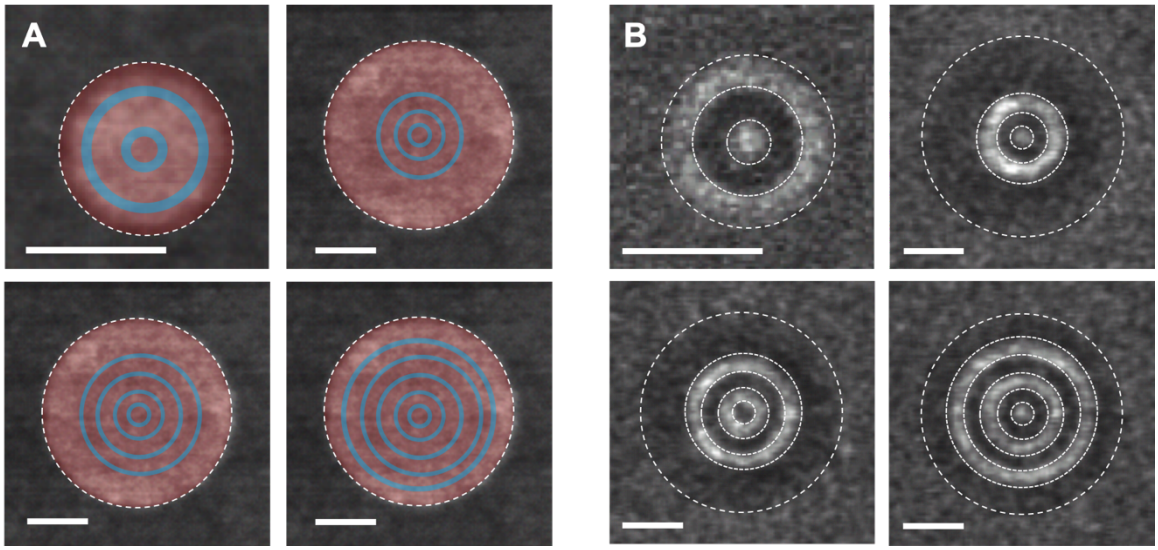

Fig. S13 Synthetic skyrmions with multiple rings. (A) False color atomic force microscopy images of synthetic skyrmions with 2, 3, 4 and 5 IP rings. The red and blue areas represent OOP and IP regions, respectively. (B) MFM images of the skyrmions with multiple rings after applying a field $-H_z$, which sets the magnetization direction in the largest OOP region. The scale bars are 500 nm.

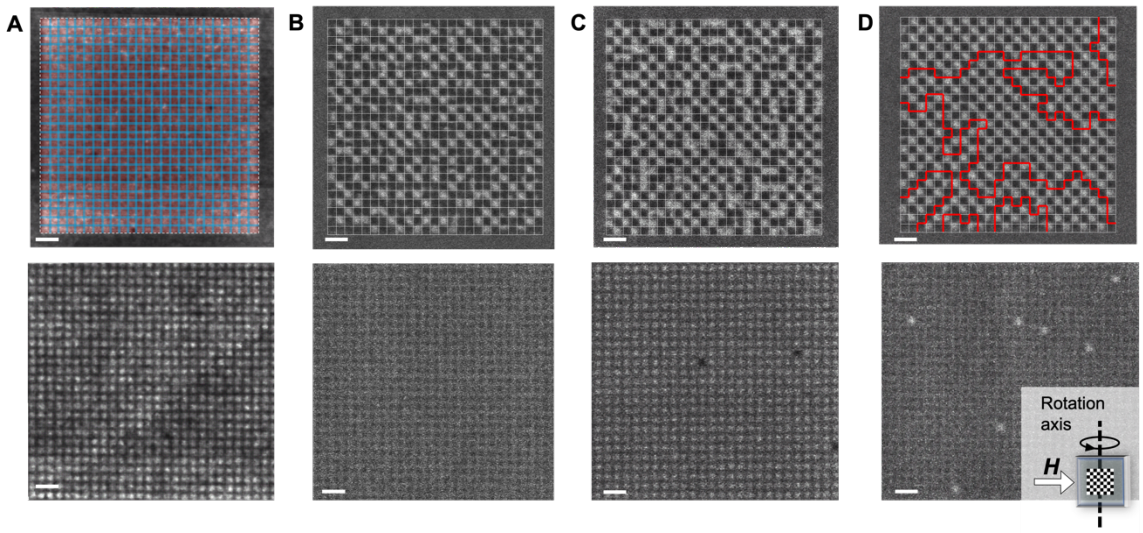

Fig. S14 Chirally coupled artificial OOP Ising spins on a square lattice. (A) Top panel: Atomic force microscopy image of a square lattice with OOP elements (red) coupled by IP elements (blue). Bottom panel: Control structure with OOP elements only. MFM images of the chirally coupled OOP elements on a square lattice (top panels) and control structure (bottom panels) after applying an out-of-plane magnetic field (B) $-H_z$, (C) $+H_z$, and (D) after rotating the sample in a magnetic field as indicated in the inset. The bright and dark MFM contrast corresponds to the magnetization pointing ↑ and ↓, respectively. The main domain boundaries are indicated by red lines in D. The scale bars are 500 nm.

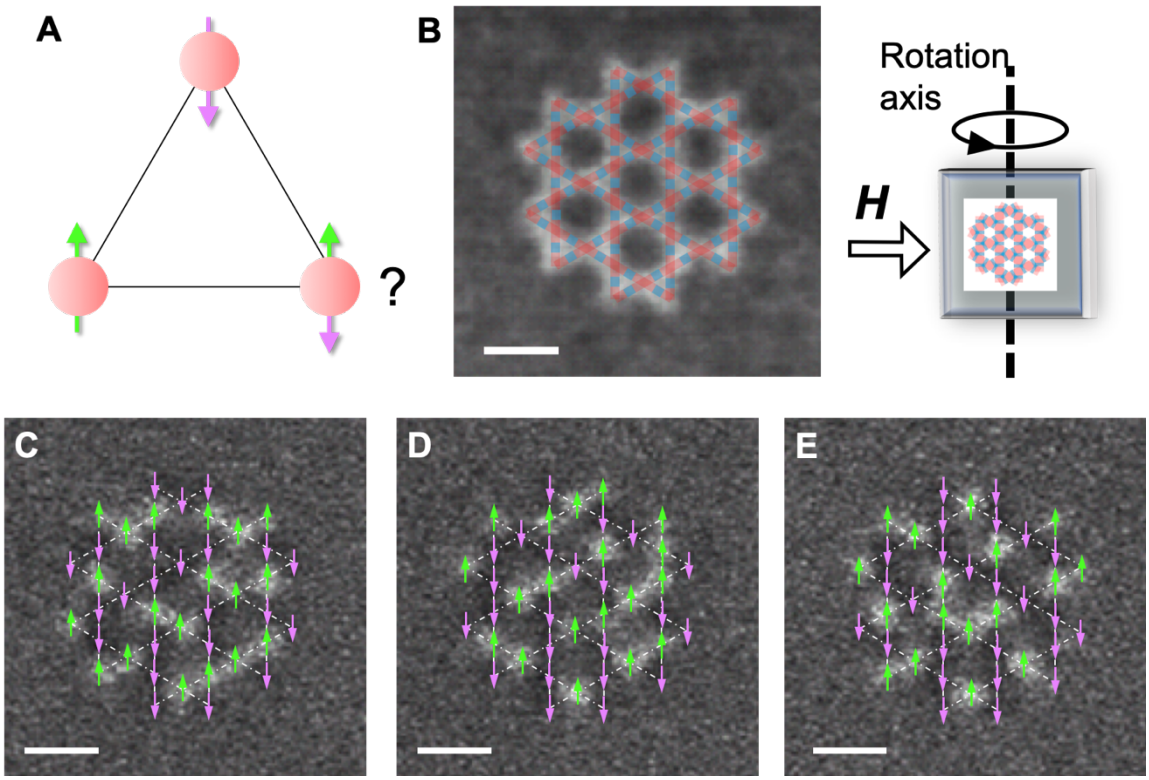

Fig. S15 Chirally coupled artificial OOP Ising spins on a kagome lattice. (A) Schematic of frustrated antiferromagnetically coupled spins on a triangle. (B) Atomic force microscopy image of an artificial kagome spin system with superimposed colors. Red indicates the position of the OOP vertices and blue indicates the IP connectors. (C) to (F) MFM images of different remanent states recorded after demagnetization by rotating the sample in a magnetic field about the axis indicated in the inset of (B). Green arrows indicate OOP elements pointing ↑ (bright MFM contrast) and purple arrows indicate OOP elements pointing ↓ (dark MFM contrast). The scale bars are 500 nm.

References and Notes

1. P. Grünberg, R. Schreiber, Y. Pang, M. B. Brodsky, H. Sowers, Layered magnetic structures: Evidence for antiferromagnetic coupling of Fe layers across Cr interlayers. *Phys. Rev. Lett.* **57**, 2442–2445 (1986). doi:10.1103/PhysRevLett.57.2442 Medline

2. S. S. Parkin, N. More, K. P. Roche, Oscillations in exchange coupling and magnetoresistance in metallic superlattice structures: Co/Ru, Co/Cr, and Fe/Cr. *Phys. Rev. Lett.* **64**, 2304–2307 (1990). doi:10.1103/PhysRevLett.64.2304 Medline

3. R. A. Duine, K. J. Lee, S. S. P. Parkin, M. D. Stiles, Synthetic antiferromagnetic spintronics. *Nat. Phys.* **14**, 217–219 (2018). doi:10.1038/s41567-018-0050-y Medline

4. M. N. Baibich, J. M. Broto, A. Fert, F. Nguyen Van Dau, F. Petroff, P. Etienne, G. Creuzet, A. Friederich, J. Chazelas, J. Chazelas, Giant magnetoresistance of (001)Fe/(001)Cr magnetic superlattices. *Phys. Rev. Lett.* **61**, 2472–2475 (1988). doi:10.1103/PhysRevLett.61.2472 Medline

5. G. Binasch, P. Grünberg, F. Saurenbach, W. Zinn, Enhanced magnetoresistance in layered magnetic structures with antiferromagnetic interlayer exchange. *Phys. Rev. B Condens. Matter* **39**, 4828–4830 (1989). doi:10.1103/PhysRevB.39.4828 Medline

6. J. Nogués, I. K. Schuller, Exchange bias. *J. Magn. Magn. Mater.* **192**, 203–232 (1999). doi:10.1016/S0304-8853(98)00266-2

7. B. Dieny, V. S. Speriosu, S. S. P. Parkin, B. A. Gurney, D. R. Wilhoit, D. Mauri, Giant magnetoresistive in soft ferromagnetic multilayers. *Phys. Rev. B Condens. Matter* **43**, 1297–1300 (1991). doi:10.1103/PhysRevB.43.1297 Medline

8. S. S. Parkin, K. P. Roche, M. G. Samant, P. M. Rice, R. B. Beyers, R. E. Scheuerlein, E. J. O'Sullivan, S. L. Brown, J. Bucchigano, D. W. Abraham, Y. Lu, M. Rooks, P. L. Trouilloud, R. A. Wanner, W. J. Gallagher, Exchange-biased magnetic tunnel junctions and application to nonvolatile magnetic random access memory. *J. Appl. Phys.* **85**, 5828–5833 (1999). doi:10.1063/1.369932

9. R. P. Cowburn, M. E. Welland, Room temperature magnetic quantum cellular automata. *Science* **287**, 1466–1468 (2000). doi:10.1126/science.287.5457.1466 Medline

10. A. Imre, G. Csaba, L. Ji, A. Orlov, G. H. Bernstein, W. Porod, Majority logic gate for magnetic quantum-dot cellular automata. *Science* **311**, 205–208 (2006). doi:10.1126/science.1120506 Medline

11. R. F. Wang, C. Nisoli, R. S. Freitas, J. Li, W. McConville, B. J. Cooley, M. S. Lund, N. Samarth, C. Leighton, V. H. Crespi, P. Schiffer, Artificial 'spin ice' in a geometrically frustrated lattice of nanoscale ferromagnetic islands. *Nature* **439**, 303–306 (2006). doi:10.1038/nature04447 Medline

12. L. J. Heyderman, R. L. Stamps, Artificial ferroic systems: Novel functionality from structure, interactions and dynamics. *J. Phys. Condens. Matter* **25**, 363201 (2013). doi:10.1088/0953-8984/25/36/363201 Medline

13. I. Dzyaloshinsky, A thermodynamic theory of "weak" ferromagnetism of antiferromagnetics. *J. Phys. Chem. Solids* **4**, 241–255 (1958). doi:10.1016/0022-3697(58)90076-3

14. T. Moriya, Anisotropic superexchange interaction and weak ferromagnetism. *Phys. Rev.* **120**, 91–98 (1960). doi:10.1103/PhysRev.120.91

15. M. Bode, M. Heide, K. von Bergmann, P. Ferriani, S. Heinze, G. Bihlmayer, A. Kubetzka, O. Pietzsch, S. Blügel, R. Wiesendanger, Chiral magnetic order at surfaces driven by inversion asymmetry. *Nature* **447**, 190–193 (2007). doi:10.1038/nature05802 Medline

16. S. Heinze, K. von Bergmann, M. Menzel, J. Brede, A. Kubetzka, R. Wiesendanger, G. Bihlmayer, S. Blügel, Spontaneous atomic-scale magnetic skyrmion lattice in two dimensions. *Nat. Phys.* **7**, 713–718 (2011). doi:10.1038/nphys2045

17. A. Fert, N. Reyren, V. Cros, Magnetic skyrmions: Advances in physics and potential applications. *Nat. Rev. Mater.* **2**, 17031 (2017). doi:10.1038/natrevmats.2017.31

18. M. Heide, G. Bihlmayer, S. Blügel, Dzyaloshinskii-Moriya interaction accounting for the orientation of magnetic domains in ultrathin films: Fe/W (110). *Phys. Rev. B* **78**, 140403 (2008). doi:10.1103/PhysRevB.78.140403

19. J. P. Tetienne, T. Hingant, L. J. Martínez, S. Rohart, A. Thiaville, L. H. Diez, K. Garcia, J.-P. Adam, J.-V. Kim, J.-F. Roch, I. M. Miron, G. Gaudin, L. Vila, B. Ocker, D. Ravelosona, V. Jacques, The nature of domain walls in ultrathin ferromagnets revealed by scanning nanomagnetometry. *Nat. Commun.* **6**, 6733 (2015). doi:10.1038/ncomms7733 Medline

20. A. Thiaville, S. Rohart, E. Jue, V. Cros, A. Fert, Dynamics of Dzyaloshinskii domain walls in ultrathin magnetic films. *Europhys. Lett.* **100**, 57002 (2012). doi:10.1209/0295-5075/100/57002

21. S. Emori, U. Bauer, S. M. Ahn, E. Martinez, G. S. Beach, Current-driven dynamics of chiral ferromagnetic domain walls. *Nat. Mater.* **12**, 611–616 (2013). doi:10.1038/nmat3675 Medline

22. K. S. Ryu, L. Thomas, S. H. Yang, S. Parkin, Chiral spin torque at magnetic domain walls. *Nat. Nanotechnol.* **8**, 527–533 (2013). doi:10.1038/nnano.2013.102 Medline

23. F. Ummelen, H. Swagten, B. Koopmans, Racetrack memory based on in-plane-field controlled domain-wall pinning. *Sci. Rep.* **7**, 833 (2017). doi:10.1038/s41598-017-00837-x Medline

24. Materials and methods are available as supplementary materials.

25. M. Belmeguenai, J.-P. Adam, Y. Roussigné, S. Eimer, T. Devolder, J.-V. Kim, S. M. Cherif, A. Stashkevich, A. Thiaville, Interfacial Dzyaloshinskii-Moriya interaction in perpendicularly magnetized Pt/Co/AlO_x ultrathin films measured by Brillouin light spectroscopy. *Phys. Rev. B* **91**, 180405 (2015). doi:10.1103/PhysRevB.91.180405

26. H. Yang, A. Thiaville, S. Rohart, A. Fert, M. Chshiev, Anatomy of Dzyaloshinskii-Moriya Interaction at Co/Pt Interfaces. *Phys. Rev. Lett.* **115**, 267210 (2015). doi:10.1103/PhysRevLett.115.267210 Medline

27. S. Monso, B. Rodmacq, S. Auffret, G. Casali, F. Fettar, B. Gilles, B. Dieny, P. Boyer, Crossover from in-plane to perpendicular anisotropy in Pt/CoFe/AlO_x sandwiches as a function of Al oxidation: A very accurate control of the oxidation of tunnel barriers. *Appl. Phys. Lett.* **80**, 4157–4159 (2002). doi:10.1063/1.1483122

28. I. M. Miron, K. Garello, G. Gaudin, P.-J. Zermatten, M. V. Costache, S. Auffret, S. Bandiera, B. Rodmacq, A. Schuhl, P. Gambardella, Perpendicular switching of a single ferromagnetic layer induced by in-plane current injection. *Nature* **476**, 189–193 (2011). doi:10.1038/nature10309 Medline

29. M. Baumgartner, K. Garello, J. Mendil, C. O. Avci, E. Grimaldi, C. Murer, J. Feng, M. Gabureac, C. Stamm, Y. Acremann, S. Finizio, S. Wintz, J. Raabe, P. Gambardella, Spatially and time-resolved magnetization dynamics driven by spin-orbit torques. *Nat. Nanotechnol.* **12**, 980–986 (2017). doi:10.1038/nnano.2017.151 Medline

30. L. Liu, C.-F. Pai, Y. Li, H. W. Tseng, D. C. Ralph, R. A. Buhrman, Spin-torque switching with the giant spin Hall effect of tantalum. *Science* **336**, 555–558 (2012). doi:10.1126/science.1218197 Medline

31. K. Garello, I. M. Miron, C. O. Avci, F. Freimuth, Y. Mokrousov, S. Blügel, S. Auffret, O. Boulle, G. Gaudin, P. Gambardella, Symmetry and magnitude of spin-orbit torques in ferromagnetic heterostructures. *Nat. Nanotechnol.* **8**, 587–593 (2013). doi:10.1038/nnano.2013.145 Medline

32. G. Yu, P. Upadhyaya, Y. Fan, J. G. Alzate, W. Jiang, K. L. Wong, S. Takei, S. A. Bender, L.-T. Chang, Y. Jiang, M. Lang, J. Tang, Y. Wang, Y. Tserkovnyak, P. K. Amiri, K. L. Wang, Switching of perpendicular magnetization by spin-orbit torques in the absence of external magnetic fields. *Nat. Nanotechnol.* **9**, 548–554 (2014). doi:10.1038/nnano.2014.94 Medline

33. S. Fukami, C. Zhang, S. DuttaGupta, A. Kurenkov, H. Ohno, Magnetization switching by spin-orbit torque in an antiferromagnet-ferromagnet bilayer system. *Nat. Mater.* **15**, 535–541 (2016). doi:10.1038/nmat4566 Medline

34. Y. W. Oh, S. H. Chris Baek, Y. M. Kim, H. Y. Lee, K.-D. Lee, C.-G. Yang, E.-S. Park, K.-S. Lee, K.-W. Kim, G. Go, J.-R. Jeong, B.-C. Min, H.-W. Lee, K.-J. Lee, B.-G. Park, Field-free switching of perpendicular magnetization through spin-orbit torque in antiferromagnet/ferromagnet/oxide structures. *Nat. Nanotechnol.* **11**, 878–884 (2016). doi:10.1038/nnano.2016.109 Medline

35. A. van den Brink, G. Vermijs, A. Solignac, J. Koo, J. T. Kohlhepp, H. J. M. Swagten, B. Koopmans, Field-free magnetization reversal by spin-Hall effect and exchange bias. *Nat. Commun.* **7**, 10854 (2016). doi:10.1038/ncomms10854 Medline

36. K. Cai, M. Yang, H. Ju, S. Wang, Y. Ji, B. Li, K. W. Edmonds, Y. Sheng, B. Zhang, N. Zhang, S. Liu, H. Zheng, K. Wang, Electric field control of deterministic current-induced magnetization switching in a hybrid ferromagnetic/ferroelectric structure. *Nat. Mater.* **16**, 712–716 (2017). Medline

37. S. Fukami, T. Anekawa, C. Zhang, H. Ohno, A spin-orbit torque switching scheme with collinear magnetic easy axis and current configuration. *Nat. Nanotechnol.* **11**, 621–625 (2016). doi:10.1038/nnano.2016.29 Medline

38. K. S. Lee, S. W. Lee, B. C. Min, K. J. Lee, Threshold current for switching of a perpendicular magnetic layer induced by spin Hall effect. *Appl. Phys. Lett.* **102**, 112410 (2013). doi:10.1063/1.4798288

39. Z. Luo *et al*., Data from: Chirally coupled nanomagnets, Zenodo (2019); https://doi.org/10.5281/zenodo.2426253.

40. A. Vansteenkiste, J. Leliaert, M. Dvornik, M. Helsen, F. Garcia-Sanchez, B. Van Waeyenberge, The design and verification of MuMax^3. *AIP Adv.* **4**, 107133 (2014). doi:10.1063/1.4899186

41. O. Boulle, J. Vogel, H. Yang, S. Pizzini, D. de Souza Chaves, A. Locatelli, T. O. Menteş, A. Sala, L. D. Buda-Prejbeanu, O. Klein, M. Belmeguenai, Y. Roussigné, A. Stashkevich, S. M. Chérif, L. Aballe, M. Foerster, M. Chshiev, S. Auffret, I. M. Miron, G. Gaudin, Room-temperature chiral magnetic skyrmions in ultrathin magnetic nanostructures. *Nat. Nanotechnol.* **11**, 449–454 (2016). doi:10.1038/nnano.2015.315 Medline

42. B. M. McCoy, T. T. Wu, *The Two Dimensional Ising Model* (Dover, 2015).